

**TITLE: Heterozygous Nonsense Variants in the Ferritin Heavy Chain Gene  
*FTH1* Cause a Novel Pediatric Neuroferritinopathy**

**Running Head:** Pathogenic variants in *FTH1* cause a pediatric neurodegenerative disorder

**Authors and Affiliations:**

Joseph T Shieh MD PhD<sup>1,10\*</sup>, Jesus A Tintos-Hernández PhD<sup>2,10</sup>, Chaya N. Murali MD<sup>3</sup>, Monica Penon-Portmann<sup>1</sup>, Marco Flores-Mendez PhD<sup>2</sup>, Adrian Santana<sup>2</sup>, Joshua A. Bulos<sup>4</sup>, Kang Du, PhD<sup>4</sup>, Lucie Dupuis MSc<sup>5</sup>, Nadirah Damseh MD<sup>5</sup>, Roberto Mendoza-Londoño MD<sup>5</sup>, Camilla Berera<sup>1</sup>, Julieann C Lee MD<sup>6</sup>, Joanna J Phillips MD PhD<sup>6,7</sup>, César A P F Alves MD PhD<sup>8</sup>, Ivan J Dmochowski PhD<sup>4</sup> and Xilma R Ortiz-González MD PhD<sup>2,9\*\*</sup>

1. Institute for Human Genetics and Department of Pediatrics, University of California San Francisco, CA, 94143
2. Division of Neurology and Center for Mitochondrial and Epigenomic Medicine, The Children's Hospital of Philadelphia, Philadelphia, PA, 19104
3. Department of Molecular and Human Genetics, Baylor College of Medicine, Houston, TX 77030
4. Department of Chemistry, University of Pennsylvania, Philadelphia, PA 19104
5. Division of Clinical and Metabolic Genetics, The Hospital for Sick Children and University of Toronto, Toronto, Canada
6. Division of Neuropathology, Department of Pathology, University of California San Francisco, CA, 94143
7. Department of Neurological Surgery, University of California San Francisco, CA, 94143
8. Division of Neuroradiology, Department of Pediatrics, The Children's Hospital of Philadelphia
9. Epilepsy Neurogenetics Initiative (ENGIN), The Children's Hospital of Philadelphia and Department of Neurology, Perelman School of Medicine, University of Pennsylvania, Philadelphia, PA, 19104
10. These authors contributed equally to this work

**Correspondence:**

\*joseph.shieh2@ucsf.edu

\*\*ortizgonzalez@chop.edu

## Abstract

1 Ferritin, the iron storage protein, is composed of light and heavy chain subunits,  
2 encoded by *FTL* and *FTH1*, respectively. Heterozygous variants in *FTL* cause  
3 hereditary neuroferritinopathy, a type of neurodegeneration with brain iron  
4 accumulation (NBIA). Variants in *FTH1* have not been previously associated with  
5 neurologic disease. We describe the clinical, neuroimaging, and neuropathology  
6 findings of five unrelated pediatric patients with *de novo* heterozygous *FTH1*  
7 variants. Children presented with developmental delay, epilepsy, and progressive  
8 neurologic decline. Nonsense *FTH1* variants were identified using whole exome  
9 sequencing, with a recurrent *de novo* variant (p.F171\*) identified in three  
10 unrelated individuals. Neuroimaging revealed diffuse volume loss, features of  
11 pontocerebellar hypoplasia and iron accumulation in the basal ganglia.  
12 Neuropathology demonstrated widespread ferritin inclusions in the brain. Patient-  
13 derived fibroblasts were assayed for ferritin expression, susceptibility to iron  
14 accumulation, and oxidative stress. Variant *FTH1* mRNA transcripts escape  
15 nonsense-mediated decay (NMD), and fibroblasts show elevated ferritin protein  
16 levels, markers of oxidative stress, and increased susceptibility to iron  
17 accumulation. C-terminus variants in *FTH1* truncate ferritin's E-helix, altering the  
18 four-fold symmetric pores of the heteropolymer and likely diminish iron-storage  
19 capacity. *FTH1* pathogenic variants appear to act by a dominant, toxic gain-of-  
20 function mechanism. The data support the conclusion that truncating variants in  
21 the last exon of *FTH1* cause a novel disorder in the spectrum of NBIA. Targeted  
22 knock-down of mutant *FTH1* transcript with antisense oligonucleotides rescues  
23 cellular phenotypes and suggests a potential therapeutic strategy for this novel  
24 pediatric neurodegenerative disorder.  
25

## 26 Introduction

27 The transition metal iron has essential roles in biological systems and  
28 associations with human disease<sup>1</sup>. Given its range of involvement in cellular  
29 functions and its potentially toxic characteristics<sup>2</sup>, iron is highly regulated to  
30 maintain homeostasis. Ferritin is a ubiquitous, highly conserved, iron-binding  
31 protein, which can store up to 4,500 ionized iron atoms. It is the predominant iron  
32 storage protein, allowing for iron to be stored intracellularly as Fe<sup>3+</sup> and released  
33 as Fe<sup>2+</sup> when needed. Ferritin is a heteropolymer composed of light (L) and  
34 heavy (H) chains, encoded by the genes *FTL* and *FTH1*, respectively<sup>3</sup>. The *FTH1*  
35 gene is the sole gene encoding the ferritin heavy chain. The heavy chain is  
36 responsible for ferroxidase activity, and it has also been implicated in iron  
37 delivery to the brain<sup>4</sup>. Ferritin accounts for the majority of iron content in the  
38 brain, where ferritin H and L chains are distributed heterogeneously: H ferritin  
39 predominates in neurons and L ferritin in microglia<sup>5</sup>, with oligodendrocytes  
40 containing substantial amounts of both ferritin chains.

41  
42 Disruption of iron homeostasis in the brain has been linked to neurodegenerative  
43 disorders<sup>6,7</sup> and genetic disorders such as as neurodegeneration with brain iron  
44 accumulation (NBIA), which often present with insidious early-onset  
45 neurodevelopmental deficits progressing to neurodegenerative features<sup>8,9</sup>.

46 Commonly affected anatomical areas in NBIA are the basal ganglia, particularly  
47 the globus pallidum and substantia nigra. The cerebellum and cortex can also be  
48 variably involved, depending on the genetic etiology. Curiously, most genes that  
49 cause NBIA disorders do not clearly play a role in iron metabolism. The *FTL*  
50 gene, encoding the ferritin light chain, is one of the few currently established  
51 NBIA genes known to be directly involved in iron homeostasis<sup>10-15</sup>. Recent  
52 studies suggest that multiple NBIA disorders are mechanistically linked to a  
53 mitochondrial acyl carrier protein<sup>16</sup>, but overall the molecular mechanisms  
54 leading to neurodegeneration in those genetic disorders remain incompletely  
55 understood.

56  
57 Heterozygous variants in *FTL* are associated with the autosomal dominant  
58 disorder known as hereditary neuroferritinopathy (also known as NBIA3, MIM:  
59 606159)<sup>17,18</sup>. It is characterized by progressive neurologic symptoms and iron

60 accumulation, particularly in the basal ganglia. The most prominent symptoms  
61 include chorea and focal dystonia and, less often, parkinsonism<sup>13</sup>. The most  
62 common pathogenic variant in *FTL* is c.450insA, which is a founder mutation  
63 from the Cumbrian region of northern England, with a mean age of symptom  
64 onset at 39 years<sup>13,17</sup>. Neuropathology shows neuronal ferritin aggregates and  
65 neuroimaging indicates accumulation in the basal ganglia. Previous studies  
66 suggest pathogenic variants associated with *FTL* hereditary neuroferritinopathy  
67 map to the C-terminus of the L-ferritin subunit, disrupting the E-helix domain and  
68 affecting iron permeability and storage capacity<sup>19-21</sup>.

69  
70 Despite the ubiquitous nature of the ferritin heavy chain, variants in the *FTH1*  
71 gene have not yet been conclusively linked to human disease. A *FTH1* promoter  
72 variant has been reported from a single family with type 5 hemochromatosis  
73 (MIM: 615517)<sup>22</sup>, but no other *FTH1*-associated disease has been reported to  
74 date. Here, we report a novel human NBIA disorder associated with *de novo*  
75 nonsense heterozygous variants in the final exon of *FTH1* in five unrelated  
76 children with characteristic clinical and imaging findings. The variants escape  
77 NMD and lead to ferritin accumulation on neuropathology, neuroimaging findings  
78 consistent with neurodegeneration with brain iron accumulation and cellular  
79 markers of oxidative stress.

## 80 81 **Material and Methods**

### 82 83 **Human Subjects**

84 Patients presented for evaluation to the Children's Hospital of Philadelphia  
85 Neurogenetics clinic, the University of California San Francisco Medical Genetics  
86 clinic, Division of Clinical and Metabolic Genetics clinic at The Hospital for Sick  
87 Children in Toronto, and Texas Children's Hospital genetics clinic in Houston,  
88 TX. They underwent clinical neuroimaging and exome sequencing as part of the  
89 medical evaluation for neurodevelopmental delay and/or progressive neurologic  
90 symptoms. Sequencing was performed by CLIA-certified laboratories. Variants in  
91 *FTH1* were identified as candidates, considered variants of unknown significance  
92 until further information became available. Human Subjects Protocols for the  
93 study have received prior approval by the appropriate Institutional Review Boards

94 and informed consent was obtained from subjects. Primary *FTH1*-variant  
95 fibroblasts were established from probands 1, 2 and 3 for cellular studies. Control  
96 fibroblasts included the unaffected parent of proband 1 (FTH control, i.e. CTRL2)  
97 and fibroblasts from Coriell Institute (GM08400, i.e. CTRL1).

98

### 99 **Neuropathology**

100 Autopsy was performed for proband 2. The brain and spinal cord were fixed in  
101 10% buffered formalin and tissues were processed, embedded, and sectioned for  
102 histologic analysis, including hematoxylin and eosin staining and Prussian blue  
103 iron stain. Immunostaining with anti-ferritin heavy chain antibody FTH1 Abcam  
104 (Cat# ab81444) was performed on formalin-fixed, paraffin-embedded tissue  
105 sections. An automated immunostainer was used (Discovery Ultra, Ventana  
106 Medical Systems, Inc., Tucson, AZ).

107

### 108 **Cell Culture**

109 Primary fibroblast lines were maintained in Dulbecco's modified Eagle's medium  
110 (DMEM; Life Technologies) supplemented with Glutamax media, 10-15% fetal  
111 bovine serum (FBS), 2 mM L-glutamine, 2.5 mM pyruvate, and non-essential  
112 amino acids (NEAAs). Fibroblasts were cultured at 37°C under a humidified  
113 atmosphere of 5% CO<sub>2</sub>. While not exceeding passage 15, cells with comparable  
114 passage numbers were used for all experiments. Fibroblast genotypes were as  
115 follows: proband 1 (P1) *FTH1* c.487\_490dupGAAT (p.S164\*); probands 2 and 3  
116 (P2 and P3) *FTH1* c.512\_513delTT p.(F171\*); and non-variant controls.

### 117 **Immunoblots**

118 Cells were washed in cold PBS and sonicated twice for 10 seconds in cold lysis  
119 buffer (30% CHAPS, 120 mM NaCl, 40 mM HEPES pH 7.5, 50 mM NaF, 2 mM  
120 NaVO<sub>3</sub>, protease inhibitor cocktail [CST 5871]). Protein concentration was  
121 measured with the Bradford reagent (Bio-Rad). Cell lysates (30 µg) were  
122 suspended in Laemmli sample buffer (Bio-Rad 161-0737), and proteins were  
123 denatured at 95°C for 5 min in the presence of 10% beta-mercaptoethanol and  
124 resolved by SDS/PAGE on 12% gels. After completion of electrophoresis,  
125 proteins were transferred to PVDF mini transfer stacks (Invitrogen, IB24002),  
126 using the iBlot™ 2 Dry Blotting System [Invitrogen, IB21001] with the following

127 blotting parameters: 20 V for 1 min, 23 V for 4 min, 25 V for 2 min. Blots were  
128 stained with Ponceau Red to confirm protein transfer. Blots were then saturated  
129 with 5% skim milk in PBS containing 0.1% (v/v) Tween 20 (PBS-T) and probed  
130 overnight with antibodies directed against FTH (Thermo Fisher Scientific, PA5-  
131 19058; 1:1000) or FTL (AB clonal, A1768; 1:1000). Following a wash with PBS-  
132 T, the blots were incubated with Near-Infrared (NIR) fluorescent secondary  
133 antibodies; IRDye® 680LT Donkey anti-Goat IgG (H + L) and IRDye® 800CW  
134 Donkey anti-Rabbit IgG (H + L) [Li-cor, 1:5000 dilution]. Normalization of targets  
135 was done by GAPDH (CST, 97166; 1:1000). Immuno-stained bands were  
136 detected with the Odyssey NIR Western Blot detection system and quantified by  
137 densitometric scanning using the ImageStudio Lite software (Li-Cor  
138 Biosciences).

### 139 **Gene Expression Studies**

140 Total RNA was extracted with the RNeasy Mini Kit (QIAGEN) and DNase-treated  
141 with TURBO DNA-free Set (Thermo Fisher Scientific, AM1907) to remove  
142 contaminating DNA from RNA preparations according to manufacturer's protocol.  
143 The concentration and purity of total RNA were assessed with a NanoDrop 8000  
144 spectrophotometer (Thermo Fisher Scientific). mRNAs were then reverse  
145 transcribed from 1 µg total RNA with SuperScript IV First-Strand Synthesis  
146 System (Thermo Fisher Scientific, 18091050) and random priming according to  
147 the manufacturer's instructions. Quantitative RT-PCR (qRT-PCR) was carried out  
148 in a 10µL reaction mixture with a 384 well format using PowerUp™ SYBR™  
149 Green Master Mix (Thermo Fisher Scientific, A25742) according to the  
150 manufacturer's protocol. Specific primer pairs were as follows: TfR primer  
151 (forward primer, 5'-CAGCCCAGCAGAAGCATT-3'; reverse primer, 5'-  
152 CCAAGAACCGCTTTATCCAG-3'), *FTL* primer (forward primer, 5'-  
153 ACCATGAGCTCCAGATTCGTC-3'; reverse primer, 5'-  
154 CACATCATCGCGGTCGAAATAG-3'), *FTH1* primer (forward primer, 5'-  
155 TCAAGAAACCAGACTGTGATGA-3'; reverse primer, 5'-  
156 AGTTTGTGCAGTTCCAGTAGT-3'), *B2M* (internal control gene) primer (forward  
157 primer, 5'-CCAGCGTACTCCAAAGATTCA-3'; reverse primer, 5'-  
158 TGGATGAAACCCAGACACATAG-3'). Real-time PCR comprised an initial  
159 denaturation at 95°C for 10 min, 40 cycles at 95°C for 15 s and 60°C for 60 s and

160 then a melt curve stage of 95°C for 15 s, 60°C for 60 s and 95°C for 15 s.  
161 Procedures were performed in triplicate and data were averaged.  
162 To specifically detect the level of mutant mRNA expressed, a multiplexed locked  
163 nucleic acid (LNA) probe-based real-time PCR was designed against the  
164 duplication (dupGAAT from proband 1). LNA oligonucleotide monomers are  
165 modified with an additional methylene bridge between 2' oxygen and 4' carbon of  
166 the ribose ring<sup>23</sup>. The modified LNA monomers allowed the development of a  
167 short (16-nt) probe, which improved sensitivity and specificity to detect mutated  
168 allele expressed transcripts. Oligonucleotides containing LNA were obtained from  
169 IDT. The sequences of the primers used are as follows: WT\_ *FTH1* allele (forward  
170 primer, 5'-TGACCACGTGACCAACTT -3'; reverse primer, 5'-  
171 CTTAGCTTTCATTATCACTGTCTC; Probe 5'-  
172 /YakYel/CAAGCCAGA/ZEN/TTCGGGCGCTCC/3IABkFQ/3'). Proband 1 *FTH*  
173 c.487\_490dupGAAT (5'-TACCTGAATGAGCAGGTGAAAG-3'; Reverse 5'-  
174 AAGAGATATTCCGCCAAGCC-3'; Probe 5'-/FAM/  
175 AGCGCCCG+A+A+TG+A+A+TC/3IABkFQ/-3'), where + represents ribose-  
176 modified LNA. Each reaction was normalized utilizing B2M Hs.PT.58v.18759587  
177 (IDT). Multiplexed qRT-PCR reaction was performed at a final volume of 10 µL.  
178 Primers were used at the concentration of 400 nM, wild type and mutant probe at  
179 250 nM, each, and 90 ng of cDNA with a 1X PrimeTime Gene Expression Master  
180 Mix (IDT 1055771).

181

## 182 **Immunocytochemistry**

183 Immunofluorescence studies were performed using human primary fibroblasts  
184 grown on UV-treated glass coverslips in a 24-well plate. Cells were washed with  
185 PBS, fixed with 4% paraformaldehyde for 15 min at room temperature (RT) and  
186 permeabilized with 0.1% Tween-20 in 10% normal goat serum (Thermo Fisher  
187 50062Z) for 1 h. Primary antibodies: Rabbit anti-FTL (AB Clonal A1768, Goat  
188 anti-FTH (Thermo Fisher PA5-19058), mouse anti-LAMP1 (DHSB, H4A3). After  
189 incubation with primaries overnight at 4°C, cells were washed 3 times and then  
190 incubated with Alexa Fluor® secondary antibodies (Thermo Fisher) for 1 h at RT,  
191 then washed 3 times with PBS and mounted on a glass slide using ProLong™  
192 Gold Antifade (Thermo Fisher). Images were acquired with LSM710 (Zeiss)



193 confocal microscope and the maximum intensity projection in the z axis (5  $\mu\text{m}$ )  
194 shown.

### 195 **Intracellular Iron Quantification**

196 Cellular iron content was assayed by inductively coupled plasma optical emission  
197 spectroscopy (ICP-OES), using a Spectro Genesis ICP-OES instrument. Sample  
198 preparation was done as follows: To primary fibroblast pellets in a 15 mL  
199 centrifuge tube, 200  $\mu\text{L}$  70% w/w  $\text{HNO}_3$  was added. After thorough mixing on a  
200 vortex mixer, the suspension was incubated in a water bath at 50°C for 12 h.  
201 After cooling to RT, the resulting solution was added to 4.8 mL deionized water  
202 and thoroughly mixed on a vortex mixer to give a sample ready for analysis. In a  
203 typical experiment, iron-specific emissions at 238.204, 239.562, 259.941 nm  
204 were independently monitored. Signal intensities of the three emission lines for a  
205 series of standard solutions containing 0, 5.1994, 19.3728, 50.986, 118.237,  
206 190.891, 502.560, 715.113, 1010.78 ppb iron were used to construct three  
207 respective linear calibrations. Reported iron concentrations are averages of  
208 values obtained from the three calibrations. Protein content was assayed for  
209 each sample and used to normalize iron content values (protein concentration in  
210  $\mu\text{g}/\text{mL}$ ). For all experiments, cells were counted and plated at same density on  
211 day 0. For iron treatment, 150  $\mu\text{g}/\text{mL}$  of FAC (ferric acid citrate, Sigma) was used  
212 for either 3 or 7 days in culture before assaying iron content. To control for  
213 different cell density/growth amongst cell lines, an aliquot of all cell pellets was  
214 taken prior to iron quantification for protein quantification, which was later used to  
215 normalize iron content to protein content per sample.

216

### 217 **Protein Oxidation Assays**

218 An OxyBlot™ Protein Oxidation Detection Kit (Sigma-Aldrich S7150) was used  
219 for immunodetection of carbonyl groups, which is a hallmark of the oxidation  
220 status of proteins introduced by oxidative reactions, following the manufacturer's  
221 directions. Briefly, two aliquots of each specimen were used. One aliquot was  
222 used as a negative control and the other was subjected to conversion to 2,4-  
223 dinitrophenylhydrazone (DNP-hydrazone) derivative through reaction with 2,4-  
224 dinitrophenylhydrazine (DNPH). Equal amounts (20  $\mu\text{g}$ ) of proteins were  
225 denatured with SDS (final concentration of 6%) and treated with 1X DNPH



226 solution (20 min) to induce derivatization. Samples designated as negative  
227 controls were treated with derivatization-control solution. After incubation,  
228 neutralization solution was added to derivatized and negative control samples.  
229 Both the treated sample and the negative control were loaded and separated by  
230 SDS-PAGE using 12% gels. Sized proteins were transferred, as described  
231 above, to a PVDF membrane, non-specific sites were blocked by incubation with  
232 blocking/dilution buffer (1% BSA/PBS-T) for 1 h under gentle shaking. Anti-DNP  
233 antibody (1:150, Sigma-Aldrich 90451) was added for 1 h at RT. Following 2  
234 washes with PBS-T, blots were incubated with NIR fluorescent secondary  
235 antibody: IRDye® 800CW Donkey anti-Rabbit IgG (H + L) [Li-cor, 1:5000  
236 dilution]. Normalization was done by total amount of protein sample per lane,  
237 using the REVERT™ Total Protein Stain Kit [LI-COR, P/N 926-11010]. Immuno-  
238 stained bands were detected with the Odyssey NIR Western Blot Detection  
239 system and quantified by densitometric scanning using the ImageStudio Lite  
240 software.

241

#### 242 **Lipid Peroxidation Assays**

243 Ten thousand cells per well were seeded in a UV transparent flat-bottomed 96-  
244 well plate (Corning 3635). Lipid peroxidation (LPO) was measured using C11-  
245 BODIPY<sup>581/591</sup> fluorescent dye, which shifts fluorescence emission when the  
246 polyunsaturated butadienyl portion of the molecule undergoes oxidation (Life  
247 technologies D3861). Cells were incubated for 30 min with 10 μM dye in PBS.  
248 Fluorescence was measured using a plate reader (SYNERGY H1) by  
249 simultaneous acquisition, samples were excited at 485 nm and emission was  
250 collected at 520/590 nm.

251

#### 252 **Anti-Sense Oligonucleotide (ASO) Experiments**

253 Custom designed 16-mer gapmer ASOs targeting the mutant  
254 *FTH1* mRNA (c.487\_490\_dup\_gaat), were synthesized comprised of sugar-  
255 modified LNAs and phosphorothioate bonds in between nucleotides. LNA sugars  
256 were introduced at the 5'- and 3'-end of the oligo using a 3LNA-10-3LNA pattern.  
257 The sugar-modified LNAs (+) were used to increase binding affinity and nuclease  
258 stability of gapmers, while phosphorothioate (\*) DNA was employed to elicit  
259 RNase H cleavage of the target<sup>24</sup>. LNA gapmer ASO,

260 5'+A\*A\*G\*c\*c\*a\*g\*a\*t\*t\*c\*a\*t\*+T\*C\*+G 3' and scramble 5'  
261 +G\*+T\*+A\*T\*a\*t\*c\*c\*a\*g\*a\*t\*a\*+c\*+G\*+C 3' were purchased from Integrated  
262 DNA Technologies (IDT). Cells were plated as described above for 24 h before  
263 transfection. Gymnotic LNA-ASO delivery was achieved using a 3 µM  
264 oligonucleotide concentration in complete cell culture medium. Cells were  
265 harvested for Western blot or RNA analysis 3 days after transfection. For lipid  
266 peroxidation studies, cells were harvested after 6 days of ASO treatment.

267

## 268 **Protein Modeling**

269 FTH1 wildtype and FTH1 mutations were modeled in PyMOL based on the X-ray  
270 crystal structure of human heavy chain apo-ferritin (PDB ID: 5N27) including  
271 annotation of E-helix.

272

273

## 274 **Results**

### 275 **Clinical Presentation\***

276 *\*in compliance with medrxiv policy, exact ages, family relations, ethnic*  
277 *background and clinical presentation details were edited/removed as requested.*  
278 *Data available by contacting corresponding author.*

279

280 In brief, all five probands presented during early childhood with moderate to  
281 severe global developmental delay, with progressive spasticity, gait difficulties  
282 and ataxia. All probands were unrelated and from diverse ethnic backgrounds,  
283 including European, African American and South Asian. Imaging was consistent  
284 with pontocerebellar hypoplasia during infancy and later evolved to show  
285 evidence of mineralization suggestive of iron accumulation. Progressive cerebral  
286 volume loss was evident in patients that underwent serial imaging over time.  
287 Table 1 summarizes the salient clinical and neuroimaging features of the patient  
288 cohort.

289

### 290 **Exome Results**

291 Exome sequencing was performed. Heterozygous *FTH1* variants were found in  
292 all five unrelated probands, with four probands sharing a recurrent variant.  
293 Additional rare variants were also considered as candidates but were not shared  
294 among the affected individuals. The *de novo* nature of the *FTH1* variants was

295 confirmed in all four probands where trio analysis could be performed. Proband 1  
296 had a novel heterozygous, *de novo* variant c.487\_490dupGAAT (p.S164\*) in  
297 *FTH1*, reported by the clinical laboratory as a candidate. She was also found to  
298 carry a paternally inherited variant of unknown significance (p.R253W) in the  
299 *TOE1* gene, which is associated with a recessive form of pontocerebellar  
300 hypoplasia (PCH7). The copy number variant of unknown significance (*IMMP2L*  
301 deletion) was found to be inherited from an asymptomatic parent. Patient 2 had a  
302 novel heterozygous, *de novo*, *FTH1* variant c.512\_513delTT, (p.F171\*), found  
303 using clinical exome sequencing, identifying a candidate gene. Two other *de*  
304 *novo* gene variants were found with low quality and there was no human disease  
305 correlate. Probands 3, 4, and 5 were found to have the same recurrent *FTH1*  
306 variant as proband 2, c.512\_513delTT (p.F171\*), although all these individuals  
307 were unrelated. The variant was confirmed as *de novo* in probands 4 and 5 as  
308 well. Proband 3 underwent a duo exome, as a paternal sample was not available;  
309 the variant was not found in the maternal sample. Given the c.512\_513delTT,  
310 (p.F171\*) variant was found in four out of five affected individuals in the cohort,  
311 the variant was suspected to be the top candidate. *FTH1* has four exons, and all  
312 variants in the probands occurred in the last exon.

313

314 The recurrent dinucleotide deletion c.512\_513delTT, leading to p.F171\*, was not  
315 present in gnomAD v.2.1.1. or v.3.1.2., nor was the dup variant  
316 c.487\_490dupGAAT leading to p.S164\*. Genic intolerance to variation in the  
317 population data also suggested the gene's potential importance. Both variants  
318 were in the final exon of the *FTH1* coding sequence suggesting likely escape  
319 from NMD. In addition, occurring in the final exon of *FTH1*, the variants are  
320 predicted to lead to a truncated C-terminus (~12-20 amino acids) in the *FTH1*  
321 protein.

322

### 323 **Distinct Neuroimaging Overlapping with PCH and NBIA syndromes**

324 Several distinct neuroimaging findings were identified in the probands with  
325 stopgain variants in the final exon of *FTH1*. Brain imaging of proband 1 (Figure  
326 1A-D) showed marked areas of abnormal iron deposition along with gliotic  
327 changes involving the anterior segment of the globus pallidi, giving the so-called  
328 eye of the tiger sign (Figure 1C). Moreover, additional findings including

329 progressive volume loss involving the cerebellum, particularly the vermis, and  
330 interval appearance of volume loss and signal changes in the supratentorial  
331 white matter were noted over time when serial imaging was reviewed (baseline  
332 imaging shown Figure 1D). Similarly, serial imaging of proband 2 also  
333 demonstrated progressive volume loss, persistent basal ganglia signal  
334 abnormalities and cerebellar hypoplasia. Imaging for proband 3 was remarkable  
335 for areas of abnormal iron mineral deposition that were noted in the basal ganglia  
336 as early as the first MRI performed before 1 year of age. The signal changes  
337 were not selective to any structure in the basal ganglia and were better observed  
338 in the gradient echo, and magnetization transfer T1 sequences. Noteworthy  
339 additional imaging features are shown from MRI around four years later,  
340 including severe pontocerebellar hypoplasia with severe atrophy of the midbrain  
341 in the axial plane giving the “figure 8” appearance (Figure 1H), along with T2  
342 crossed linear hyperintensities, representing selective degeneration of transverse  
343 pontocerebellar tracts and median pontine raphe nuclei (“hot cross bun sign”)  
344 (Figure 1I). The “hot cross” bun sign represents a classic imaging pattern related  
345 to other neurodegenerative disorders, particularly the cerebellar subtype of  
346 multiple system atrophy, and different types of spinocerebellar ataxia<sup>25</sup>. The  
347 association between pontocerebellar hypoplasia and imaging features of axonal  
348 tract degeneration (hot-cross bun sign) involving the pons suggest that this  
349 disease has a progressive course likely with a prenatal onset. Additional findings  
350 including severe white matter volume loss particularly involving the frontal,  
351 parietal, and temporal lobes along with diffusely thin corpus callosum were also  
352 noted (Figure 1E-G).

353

354 Selective cerebellar atrophy, particularly involving the vermis, with or without the  
355 involvement of the brainstem, along with progressive white matter volume loss  
356 and evidence of iron deposition in the basal ganglia in the early stages of the  
357 disease represent the most common imaging findings in the patients imaged with  
358 *FTH1* variants. Overall, for cases reviewed, the supratentorial atrophy appears  
359 mainly related to white matter volume loss. Moreover, additional imaging markers  
360 including the eye of the tiger sign in the globus pallidi and the hot cross bun sign  
361 in the pons were noted in some of the patients, evincing that these findings are

362 not necessarily pathognomonic for PKAN and multiple system atrophy type C,  
363 respectively.

364

### 365 **Pathological Findings**

366 Neuropathological studies were performed for Proband 2, who died of  
367 complications of the disease in her 20s. She experienced dysphagia, weight  
368 loss, menorrhagia, and lethargy, and despite transfusion, hospitalization and  
369 stabilization, she continued to decline and signs of pneumonia were found on  
370 autopsy. There was diffuse and extensive involvement of brain, brainstem, and  
371 spinal cord with striking involvement, and patchy destruction, of the basal ganglia  
372 and midbrain, including the red nucleus and substantia nigra. Eosinophilic  
373 intracytoplasmic and intranuclear inclusions were present diffusely (Figure 2A),  
374 including NeuN positive neurons (Figure 2B). Extracellular deposits were  
375 particularly prominent in the white matter and basal ganglia, where Prussian blue  
376 staining revealed patchy iron deposition (Figure 2C). Inclusions were also found  
377 in the cortex and cerebellum. The eosinophilic inclusions and deposits were  
378 diffusely immunopositive for FTH1 (Figure 2D). Pathological analyses revealed  
379 rare iron staining in the gastrointestinal system, suggesting other cells outside of  
380 the nervous system may be subtly affected.

381

### 382 ***FTH1* Transcripts and Increase in Cellular Ferritin Protein Levels**

383 As all variants identified in the patients were nonsense variants predicted to lead  
384 to premature protein truncation<sup>26</sup>. Truncating variants in the last exon of a gene  
385 are typically expected to escape nonsense mediated decay (NMD). We first  
386 assayed total *FTH1* mRNA and protein levels in patient fibroblasts compared to  
387 control lines. Both heavy (Figure 3A) and light chain (Figure 3B) ferritin protein  
388 levels were elevated in patient fibroblasts relative to controls. Therefore, *FTH1*-  
389 variant cells demonstrate an increase in ferritin heavy chain protein levels, which  
390 suggests the variant mRNA transcript does not lead to haploinsufficiency. To  
391 determine how *FTH1* variants affected total *FTH1* transcript levels, we assayed  
392 mRNA levels by RT-PCR. *FTH1* mRNA expression levels were reduced in patient  
393 cells vs controls, by around 20 percent (P1=78% of control, P2=83%, Figure 3C).  
394 *FTL* mRNA transcript levels were either lower or unchanged in patient cells, only  
395 statistically significant in the P2 line. The results suggest other mechanisms

396 influencing ferritin protein levels beyond mRNA translation, which could include  
397 posttranslational regulatory mechanisms and/or effects of the variants in protein  
398 stability or regulation<sup>27</sup>.

399

400 To further determine whether the mutant transcripts are able to escape nonsense  
401 mediated decay, we designed mutant specific primers for each variant  
402 (c.487\_490dupGAAT for P1 and c.512\_513delTT for P2). We quantified wild type  
403 vs mutant transcripts simultaneously by RT-PCR. Mutant-specific mRNA  
404 transcripts were readily detectable in patient-derived cells and not in controls  
405 (Figure 3D) demonstrating escape from NMD. Mutant mRNA transcripts were  
406 not only clearly detectable, but in the case of P1, mutant transcript levels were  
407 higher than those of the wild type allele.

408

409 In order to evaluate the subcellular localization of ferritin heavy chain, *FTH1*  
410 patient fibroblasts were immunostained using anti-ferritin light and heavy chain  
411 antibodies, as well as the lysosomal marker LAMP1. Ferritin can be degraded in  
412 the lysosome, also known as ferritinophagy. Fibroblasts showed ferritin signal in  
413 the expected predominant cytoplasmic distribution, with aggregate-like structures  
414 visible in patient cells (Figure 4C) and not in control (Figure 4A). Iron exposure  
415 with ferric ammonium citrate (FAC) for 3 days led to expected increase in ferritin  
416 signal in both control (Figure 4B) and patient cells (Figure 4D); ferritin staining  
417 and aggregate-like structures were more robust in patient cells. We did not  
418 observe significant colocalization of heavy nor light chain ferritin in lysosomes in  
419 fibroblasts (Figure 4A-D).

420

#### 421 **Cellular Iron Content and Susceptibility to Oxidative Stress**

422 Elemental iron content was measured by the highly sensitive technique of  
423 inductively coupled plasma optical emission spectroscopy (ICP-OES), at baseline  
424 and after iron treatment (FAC, ferric acid citrate 150 µg/mL). No significant  
425 differences in iron content were detected in patient fibroblasts at baseline, when  
426 tested up to 7 days in culture (Figure 5A, untreated controls shown as lower dark  
427 grey bars). With iron exposure, as expected, all cell lines showed statistically  
428 significant increases in iron content (by 3, 7 days) relative to respective untreated  
429 controls (top bars). Nevertheless, there was no significant difference in iron

430 content in control vs patient fibroblasts assayed at days 1 or 3 of treatment. At 7  
431 days of iron exposure, the p.S164\* variant cells showed a significant increase in  
432 iron content relative to controls, but there was no significant difference between  
433 the two p.F171\* cell lines and controls, suggesting there may be variability in the  
434 cellular effects of the ferritin variants.

435

436 Because cellular iron dysregulation can be associated with oxidative stress and  
437 is hypothesized to be relevant to neurodegenerative processes<sup>19,28</sup>, we tested  
438 whether the *FTH1* cells showed signs of oxidative damage. Because increased  
439 oxidative stress is known to cause protein and lipid peroxidation, we assayed for  
440 such markers in patient cells. Oxyblot assays for protein oxidation were  
441 performed (Figure 5B), showing an increase in total oxidized proteins in P1 and  
442 P2 fibroblasts. To assess lipid peroxidation (LPO)<sup>3,29</sup>, the lipid peroxidation  
443 sensor B11-BODIPY was used. *FTH1*-mutant cells showed higher levels of  
444 peroxidized lipids compared to controls (Figure 5C), suggesting *FTH1*-variant  
445 cells demonstrate intrinsic differences in oxidative stress.

446

#### 447 **Structural Modeling Suggests *FTH1* Variants Alter Ferritin's Pore**

448 To model the potential effects of *de novo* heterozygous *FTH1* variants on the  
449 ferritin 24mer complex, we analyzed 3-dimensional structures using PyMOL and  
450 the X-ray structure for heavy ferritin chain (PDB ID: 5N27). The wild-type FTH  
451 subunit is comprised of a four  $\alpha$ -helix bundle (helices A-D) connected via a  
452 flexible loop to a shorter E-helix. The 3-dimensional protein structure changes  
453 with the p.S164\* mutation, which deletes the E-helix, while the p.F171\* mutation  
454 leads to truncation of the E-helix. Alteration of the E-helix results in malformation  
455 of the 4-fold symmetric pores, which are important for iron retention<sup>30-32</sup>. We  
456 predict from structural analysis that the pore formed by p.S164\* should be  
457 substantially larger than wild-type. This structural defect is exacerbated when all  
458 four subunits that comprise the pore have a modified E-helix (Figure 6).  
459 Interestingly, assembly of the p.F171\* subunits is predicted to minimally impact  
460 pore size at the four-fold axes. Nevertheless, for the p.F171\* variant, the depth of  
461 the pore is predicted to be 4.5 Å shallower than wild-type due to the missing  
462 terminal residues. The p.F171\* variant is also missing K173, and this positive  
463 charge is potentially important for preventing iron from leaving the ferritin cavity



464 through the pore. These changes could lead to altered pore function, ferritin  
465 structure or reduced ferritin iron binding capacity.

466

#### 467 **Allele-Specific Oligonucleotide (ASO) Rescues *FTH1* p.S164\* Variant Cells**

468 Based on our findings of elevated ferritin protein levels in patient-derived cells  
469 and RT-PCR revealing that mutant *FTH1* alleles are detectable in patient but not  
470 control cells, we hypothesized that *FTH1* variants exert a dominant negative  
471 effect by escaping NMD. Therefore, we used the allele-specific mRNA assay to  
472 test the effectiveness of an ASO designed to suppress the expression of the  
473 mutant allele in P1 cells. We selected the P1 cells as the structural (larger effect  
474 on the pore) and experimental data (significant iron accumulation upon exposure)  
475 suggested a more robust cellular phenotype for the P1 variant (p.S164\*)  
476 compared to the recurrent variant (p.F171\*). We found that mutant allele mRNA  
477 expression was suppressed with ASO treatment, but not with a scrambled control  
478 (Figure 7A). By suppressing the mutant allele in the P1 line, we could also detect  
479 diminished increase in lipid peroxidation (LPO) to control levels (Figure 7B).  
480 Furthermore, treatment with mutant-specific ASO partially rescued the elevated  
481 ferritin heavy chain protein levels in P1 cells to near control levels (Figure 7C).

482

#### 483 **Discussion**

484 This report documents a novel neurodevelopmental disorder associated with  
485 heterozygous *de novo* *FTH1* variants, with symptoms, neuroimaging and  
486 histological findings supporting a novel neuroferritinopathy. Probands presented  
487 in early childhood with neurodevelopmental delay and some later developed  
488 progressive neurological symptoms including ataxia, seizures, and spasticity.  
489 Notably, early brain imaging findings exhibited overlap with some forms of  
490 congenital pontocerebellar hypoplasia, but signal abnormalities suggesting iron  
491 accumulation became evident later in life. Our data suggest that the described  
492 *FTH1* variants exert a dominant negative effect, perhaps due to impaired ability  
493 of ferritin to store iron as the truncated E-Helix may alter ferritin's pore size  
494 (p.S164\*) or depth (p.F171\*). This appears to result in oxidative stress, as  
495 evidenced in functional validation studies in patient-derived fibroblasts.

496

497 This novel disorder is further distinguished by specific neuroimaging features,  
498 including the eye of the tiger sign, classically described in the context of PKAN<sup>33</sup>,  
499 some cases with evidence of selective degeneration of the transverse fibers of  
500 the pons and median pontine raphe nuclei, leading to the “hot cross bun” sign,  
501 and severe atrophy of the midbrain in the axial plane giving the “figure 8”  
502 appearance along with severe leukomalacia, classically seen in *AMPD2*-  
503 associated PCH type 9<sup>34</sup>. These data expand the differential diagnosis of these  
504 neuroimaging signs to include *FTH1*-associated neuroferritinopathy.

505

506 The individuals described in this study presented with neurodevelopmental  
507 delays early in life, whereas in *FTL*-associated neuroferritinopathy, symptom  
508 onset typically occurs in adulthood, first with movement disorders (mean age of  
509 onset 39 years), followed by cognitive decline<sup>17,18</sup>.

510 In addition to endogenous production in the brain, cellular systems and animal  
511 models have shown that heavy chain ferritin protein (but not L ferritin) is able to  
512 cross the blood-brain barrier<sup>35,36</sup>. The possibility that the brain may accumulate  
513 FTH from the body could potentially contribute to the childhood symptom onset in  
514 patients with *FTH1*-related disease compared to patients who present at middle  
515 age *FTL*-related disease. Additional studies would be needed to test these  
516 possibilities.

517

518 Despite different ages of onset, both disorders share imaging features such as  
519 iron accumulation and clinical evidence of neurodegeneration. The  
520 neuropathological findings in our probands with *FTH1* variants are reminiscent of  
521 those described in *FTL*-associated neuroferritinopathy, including  
522 immunohistochemical staining showing ferritin positive aggregates and iron  
523 accumulation in the brain<sup>37</sup>. *FTH1*-associated neuroferritinopathy appears to  
524 have early pontocerebellar involvement as a distinct feature. Disease models of  
525 *FTL*-associated neuroferritinopathy have also been shown to exhibit ferritin  
526 aggregates, oxidative stress and higher lipid peroxidation levels<sup>28,38,39</sup>. We found  
527 that upon iron exposure, patient-derived cells showed significantly increased  
528 levels relative to controls. A potential limitation is that fibroblasts may not  
529 completely recapitulate the effects of *FTH1* variants in other cell types,  
530 particularly neurons. In addition, the different ratios of ferritin heavy and light

531 chains in different cells could also be important. Future studies in animal and/or  
532 IPS models should examine the tissue specific-sequelae of truncating the E-helix  
533 in the central nervous system.

534

535 Similar to adults with *FTL*-associated neuroferritinopathy, our cases do not show  
536 significant systemic iron overload or overt hyperferritinemia. Serum ferritin levels  
537 were low or normal in all but one proband (Table 1). Notably, 5' non-coding  
538 variants in both *FTL* and *FTH1* have been previously associated with iron  
539 overload. In hyperferritinemia with or without cataracts (MIM 600866)<sup>15,40</sup>,  
540 heterozygous variants occur in the 5-prime non-coding *FTL* region that binds to  
541 iron regulatory elements<sup>41</sup>. It is thought that these variants result in disrupted  
542 regulation of ferritin light chain translation, leading to hyperferritinemia. In  
543 hemochromatosis type 5 (MIM 615517), a single family was reported with  
544 missense variant in the 5'-UTR of *FTH1* (p.A94U) altering affinity for IRP (iron  
545 regulatory protein) binding<sup>42</sup>. On the other hand, pathogenic variants leading to  
546 neuroferritinopathy in *FTH1* and *FTL* both show recurrent C-terminus nucleotide  
547 deletions/duplications leading to frameshift, truncating the E-Helix of the ferritin  
548 protein subunits<sup>3,38</sup>. The data here supports dominant negative action of mutant  
549 ferritin, with structural modeling data suggesting alterations in ferritin pore  
550 structure. None of the five patients had signs of hemochromatosis. However,  
551 some patients in our cohort had low serum ferritin levels (Table 1), which may be  
552 consistent with serum ferritin findings in *FTL*-neuroferritinopathy<sup>13</sup>.

553

554 Structural studies suggest that the ferritin protein E-helix is fundamental for the  
555 stability and assembly of the protein complex. Although this domain does not  
556 have a ferroxidase function nor contain an iron binding site, it can be flipped in or  
557 out of the nanocage<sup>43</sup>, thereby affecting its capacity for binding and mineralizing  
558 iron. Previous studies with *FTL* confirmed that amino acid deletions in the *FTL* C-  
559 terminus resulted in iron-induced precipitation and revealed iron mishandling<sup>30</sup>.  
560 *FTL* E-helix mutations have been linked to the formation of ferritin inclusion  
561 bodies, which highlights the significance of the wild-type E-helix in producing fully  
562 functional ferritin protein. Targeted mutagenesis studies with murine ferritin  
563 heavy chain protein have shown that truncating the E-helix contribute to poor  
564 ferritin stability and solubility and poor sequestration of cellular iron<sup>44</sup>. In

565 alignment with these previous data, the structural *in silico* data presented here  
566 predicts that C-terminal truncating variants in *FTH1* alter the E-helix, affecting  
567 ferritin pore size and/or depth, which would be expected to alter ferritin's iron  
568 storage capacity.

569

570 The data reported herein, including elevated cellular ferritin levels, detection of  
571 mutant mRNA despite nonsense variants, and the potential rescue of cellular  
572 phenotypes with targeted mutant allele knockdown with ASO, suggest that the  
573 pathogenic mechanism of the *FTH1* heterozygous variants is a dominant  
574 negative effect, as opposed to haploinsufficiency. Concordant with this, previous  
575 mouse studies demonstrate that haploinsufficiency of *Fth1* does not result in a  
576 clear phenotype<sup>45</sup>. Suppressing mutant allele expression with ASO provides  
577 proof of principle for a strategy to possibly ameliorate pathogenic *FTH1*  
578 expression in cells.

579

580 In summary, the results presented here support a new human disease  
581 association for the iron homeostatic gene, *FTH1*. Heterozygous *de novo* stopgain  
582 variants in the final exon of *FTH1* are associated with a novel pediatric  
583 neuroferritinopathy within the spectrum of NBIA disorders. Our findings suggest  
584 disease-causing *FTH1* variants lead to truncation of the E-helix of ferritin heavy  
585 chain, which alters protein function by altering the ferritin pore size and/or depth.  
586 Neuropathology confirms ferritin aggregates in the brain and widespread  
587 evidence of neurodegeneration. The data are consistent with the proposed  
588 disease mechanisms for *FTL*-associated hereditary neuroferritinopathy,  
589 suggesting some degree of shared downstream consequences, regardless of  
590 whether mutations occur in the ferritin light or heavy chain. Finally, the cellular  
591 effects of pathogenic *FTH1* variants can be modified with antisense  
592 oligonucleotides, raising the possibility that similar therapeutic approaches may  
593 be applicable for patients with neuroferritinopathy regardless of genetic etiology.

594

595

## 596 **Acknowledgements**

597 We wish to thank the patients and their families who participated in this study and  
598 also acknowledge their philanthropic support via the NBIA Fund at the Children's

599 Hospital of Philadelphia. JTS thanks the Marcus Program in Precision Medicine  
600 and the Benioff Children's Hospital, University of California San Francisco for  
601 their funding and support. IJD thanks the NSF, CHE-1905203. XOG thanks the  
602 Robert Wood Johnson Foundation (Harold Amos Faculty Development  
603 Program), NINDS (1K02NS112456-01A1) and the Burroughs Wellcome Fund  
604 (CAMS Award). Also, CHOP's Roberts Collaborative for Genetics and  
605 Individualized Medicine (to XOG). We acknowledge the UCSF Brain Tumor  
606 SPORE Biorepository (NIH/NCI P50CA097257 JJP) for providing histology  
607 services. We thank UCLA Genomics Center, GeneDx and GeneMatcher<sup>46</sup>.

608  
609

### 610 **Author Contributions**

611 JTS and XOG contributed to the conception and design of the study;  
612 JTS, JATH, CNM MPP, MFH, AS, LD, ND, RML, CB, JCL, JJP, CAPFA, IJD,  
613 XOG contributed to the acquisition and analysis of data; JTS, JATH, CNM, AS,  
614 MFH, CAPFA, XOG contributed to the drafting a significant portion of the  
615 manuscript or figures. All authors contributed to copy editing and approval.

616

### 617 **Declaration of Interests**

618 The authors declare no competing interests.

619

### 620 **Data and Code Availability**

621 The data described during this study will be made available upon reasonable  
622 request.

623

### **Social Media Summary**

The report describes *de novo* variants in *FTH1*, encoding ferritin heavy chain are linked to a novel pediatric disease in the spectrum of NBIA (neurodegeneration with brain iron accumulation). Our data suggest that C-terminus variants truncating the E-Helix of the ferritin heavy chain lead to brain ferritin accumulation and cellular oxidative stress, which can be ameliorated by antisense oligonucleotides. Twitter Handles: @drxilma, @chayasays

624

References

- 625  
626 1. Nakamura, T., Naguro, I., and Ichijo, H. (2019). Iron homeostasis and  
627 iron-regulated ROS in cell death, senescence and human diseases.  
628 *Biochim Biophys Acta Gen Subj* 1863, 1398-1409.  
629 2. Miller, C.J., Rose, A.L., and Waite, T.D. (2016). Importance of Iron  
630 Complexation for Fenton-Mediated Hydroxyl Radical Production at  
631 Circumneutral pH. *Frontiers in Marine Science* 3.  
632 10.3389/fmars.2016.00134.  
633 3. Muhoberac, B.B., and Vidal, R. (2019). Iron, Ferritin, Hereditary  
634 Ferritinopathy, and Neurodegeneration. *Front. Neurosci.* 13, 1195.  
635 10.3389/fnins.2019.01195.  
636 4. Fisher, J., Devraj, K., Ingram, J., Slagle-Webb, B., Madhankumar, A.B.,  
637 Liu, X., Klinger, M., Simpson, I.A., and Connor, J.R. (2007). Ferritin: a  
638 novel mechanism for delivery of iron to the brain and other organs. *Am. J.*  
639 *Physiol. Cell Physiol.* 293, C641-649. 10.1152/ajpcell.00599.2006.  
640 5. Connor, J.R., Boeshore, K.L., Benkovic, S.A., and Menzies, S.L. (1994).  
641 Isoforms of ferritin have a specific cellular distribution in the brain. *J*  
642 *Neurosci Res* 37, 461-465.  
643 6. Kaur, D., Yantiri, F., Rajagopalan, S., Kumar, J., Mo, J.Q., Boonplueang,  
644 R., Viswanath, V., Jacobs, R., Yang, L., Beal, M.F., et al. (2003). Genetic  
645 or pharmacological iron chelation prevents MPTP-induced neurotoxicity in  
646 vivo: a novel therapy for Parkinson's disease. *Neuron* 37, 899-909.  
647 10.1016/s0896-6273(03)00126-0.  
648 7. Puccio, H., Simon, D., Cossee, M., Criqui-Filipe, P., Tiziano, F., Melki, J.,  
649 Hindelang, C., Matyas, R., Rustin, P., and Koenig, M. (2001). Mouse  
650 models for Friedreich ataxia exhibit cardiomyopathy, sensory nerve defect  
651 and Fe-S enzyme deficiency followed by intramitochondrial iron deposits.  
652 *Nat. Genet.* 27, 181-186. 10.1038/84818.  
653 8. Di Meo, I., and Tiranti, V. (2018). Classification and molecular  
654 pathogenesis of NBIA syndromes. *Eur. J. Paediatr. Neurol.* 22, 272-284.  
655 10.1016/j.ejpn.2018.01.008.  
656 9. Meyer, E., Kurian, M.A., and Hayflick, S.J. (2015). Neurodegeneration  
657 with Brain Iron Accumulation: Genetic Diversity and Pathophysiological  
658 Mechanisms. *Annu. Rev. Genomics Hum. Genet.* 16, 257-279.  
659 10.1146/annurev-genom-090314-025011.  
660 10. Maccarinelli, F., Pagani, A., Cozzi, A., Codazzi, F., Di Giacomo, G.,  
661 Capoccia, S., Rapino, S., Finazzi, D., Politi, L.S., Cirulli, F., et al. (2015).  
662 A novel neuroferritinopathy mouse model (FTL 498InsTC) shows  
663 progressive brain iron dysregulation, morphological signs of early  
664 neurodegeneration and motor coordination deficits. *Neurobiol. Dis.* 81,  
665 119-133. 10.1016/j.nbd.2014.10.023.  
666 11. Moutton, S., Fergelot, P., Trocello, J.M., Plante-Bordeneuve, V.,  
667 Houcinat, N., Wenisch, E., Larue, V., Brugieres, P., Clot, F., Lacombe, D.,  
668 et al. (2014). A novel FTL mutation responsible for neuroferritinopathy  
669 with asymmetric clinical features and brain anomalies. *Parkinsonism*  
670 *Relat. Disord.* 20, 935-937. 10.1016/j.parkreldis.2014.04.026.  
671 12. Batey, S., Vuillaume, I., Devos, D., Destee, A., Curtis, A.J., Lombes, A.,  
672 Curtis, A., Burn, J., and Chinnery, P.F. (2010). A novel FTL insertion  
673 causing neuroferritinopathy. *J. Med. Genet.* 47, 71-72.  
674 10.1136/jmg.2008.061911.



- 675 13. Devos, D., Tchofo, P.J., Vuillaume, I., Destee, A., Batey, S., Burn, J., and  
676 Chinnery, P.F. (2009). Clinical features and natural history of  
677 neuroferritinopathy caused by the 458dupA FTL mutation. *Brain* 132,  
678 e109. 10.1093/brain/awn274.
- 679 14. Maciel, P., Cruz, V.T., Constante, M., Iniesta, I., Costa, M.C., Gallati, S.,  
680 Sousa, N., Sequeiros, J., Coutinho, P., and Santos, M.M. (2005).  
681 Neuroferritinopathy: missense mutation in FTL causing early-onset  
682 bilateral pallidal involvement. *Neurology* 65, 603-605.  
683 10.1212/01.wnl.0000178224.81169.c2.
- 684 15. Cadenas, B., Fita-Torro, J., Bermudez-Cortes, M., Hernandez-Rodriguez,  
685 I., Fuster, J.L., Llinares, M.E., Galera, A.M., Romero, J.L., Perez-Montero,  
686 S., Tornador, C., and Sanchez, M. (2019). L-Ferritin: One Gene, Five  
687 Diseases; from Hereditary Hyperferritinemia to Hypoferritinemia-Report of  
688 New Cases. *Pharmaceuticals (Basel)* 12. 10.3390/ph12010017.
- 689 16. Lambrechts, R.A., Schepers, H., Yu, Y., van der Zwaag, M., Autio, K.J.,  
690 Vieira-Lara, M.A., Bakker, B.M., Tijssen, M.A., Hayflick, S.J., Grzeschik,  
691 N.A., and Sibon, O.C. (2019). CoA-dependent activation of mitochondrial  
692 acyl carrier protein links four neurodegenerative diseases. *EMBO Mol.*  
693 *Med.* 11, e10488. 10.15252/emmm.201910488.
- 694 17. Curtis, A.R., Fey, C., Morris, C.M., Bindoff, L.A., Ince, P.G., Chinnery,  
695 P.F., Coulthard, A., Jackson, M.J., Jackson, A.P., McHale, D.P., et al.  
696 (2001). Mutation in the gene encoding ferritin light polypeptide causes  
697 dominant adult-onset basal ganglia disease. *Nat. Genet.* 28, 350-354.  
698 10.1038/ng571.
- 699 18. Chinnery, P.F., Curtis, A.R., Fey, C., Coulthard, A., Crompton, D., Curtis,  
700 A., Lombes, A., and Burn, J. (2003). Neuroferritinopathy in a French  
701 family with late onset dominant dystonia. *J. Med. Genet.* 40, e69.  
702 10.1136/jmg.40.5.e69.
- 703 19. Levi, S., and Rovida, E. (2015). Neuroferritinopathy: From ferritin  
704 structure modification to pathogenetic mechanism. *Neurobiol. Dis.* 81,  
705 134-143. 10.1016/j.nbd.2015.02.007.
- 706 20. Irimia-Dominguez, J., Sun, C., Li, K., Muhoberac, B.B., Hallinan, G.I.,  
707 Garringer, H.J., Ghetti, B., Jiang, W., and Vidal, R. (2020). Cryo-EM  
708 structures and functional characterization of homo- and heteropolymers of  
709 human ferritin variants. *Sci Rep* 10, 20666. 10.1038/s41598-020-77717-4.
- 710 21. McNally, J.R., Mehlenbacher, M.R., Lusciati, S., Smith, G.L., Reutovich,  
711 A.A., Maura, P., Arosio, P., and Bou-Abdallah, F. (2019). Mutant L-chain  
712 ferritins that cause neuroferritinopathy alter ferritin functionality and iron  
713 permeability. *Metallomics* 11, 1635-1647. 10.1039/c9mt00154a.
- 714 22. Umair, M., and Alfadhel, M. (2019). Genetic Disorders Associated with  
715 Metal Metabolism. *Cells* 8.
- 716 23. Davalieva, K., Kiprijanovska, S., and Plaseska-Karanfilska, D. (2014).  
717 Fast, reliable and low cost user-developed protocol for detection,  
718 quantification and genotyping of hepatitis C virus. *J. Virol. Methods* 196,  
719 104-112. 10.1016/j.jviromet.2013.11.002.
- 720 24. Pendergraff, H.M., Krishnamurthy, P.M., Debacker, A.J., Moazami, M.P.,  
721 Sharma, V.K., Niitsoo, L., Yu, Y., Tan, Y.N., Haitchi, H.M., and Watts, J.K.  
722 (2017). Locked Nucleic Acid Gappers and Conjugates Potently Silence  
723 ADAM33, an Asthma-Associated Metalloprotease with Nuclear-Localized  
724 mRNA. *Mol Ther Nucleic Acids* 8, 158-168. 10.1016/j.omtn.2017.06.012.



- 725 25. Zhu, S., Deng, B., Huang, Z., Chang, Z., Li, H., Liu, H., Huang, Y., Pan,  
726 Y., Wang, Y., Chao, Y.X., et al. (2021). "Hot cross bun" is a potential  
727 imaging marker for the severity of cerebellar ataxia in MSA-C. *NPJ*  
728 *Parkinsons Dis* 7, 15. [10.1038/s41531-021-00159-w](https://doi.org/10.1038/s41531-021-00159-w).
- 729 26. Inoue, K., Khajavi, M., Ohyama, T., Hirabayashi, S., Wilson, J., Reggin,  
730 J.D., Mancias, P., Butler, I.J., Wilkinson, M.F., Wegner, M., and Lupski,  
731 J.R. (2004). Molecular mechanism for distinct neurological phenotypes  
732 conveyed by allelic truncating mutations. *Nat Genet* 36, 361-369.  
733 [10.1038/ng1322](https://doi.org/10.1038/ng1322).
- 734 27. Rouault, T.A. (2002). Post-transcriptional regulation of human iron  
735 metabolism by iron regulatory proteins. *Blood Cells Mol Dis* 29, 309-314.  
736 [10.1006/bcmd.2002.0571](https://doi.org/10.1006/bcmd.2002.0571).
- 737 28. Barbeito, A.G., Garringer, H.J., Baraibar, M.A., Gao, X., Arredondo, M.,  
738 Nunez, M.T., Smith, M.A., Ghetti, B., and Vidal, R. (2009). Abnormal iron  
739 metabolism and oxidative stress in mice expressing a mutant form of the  
740 ferritin light polypeptide gene. *J. Neurochem.* 109, 1067-1078.  
741 [10.1111/j.1471-4159.2009.06028.x](https://doi.org/10.1111/j.1471-4159.2009.06028.x).
- 742 29. Shchepinov, M.S. (2020). Polyunsaturated Fatty Acid Deuteration against  
743 Neurodegeneration. *Trends Pharmacol. Sci.* 41, 236-248.  
744 [10.1016/j.tips.2020.01.010](https://doi.org/10.1016/j.tips.2020.01.010).
- 745 30. Baraibar, M.A., Muhoberac, B.B., Garringer, H.J., Hurley, T.D., and Vidal,  
746 R. (2010). Unraveling of the E-helices and disruption of 4-fold pores are  
747 associated with iron mishandling in a mutant ferritin causing  
748 neurodegeneration. *J Biol Chem* 285, 1950-1956.  
749 [10.1074/jbc.M109.042986](https://doi.org/10.1074/jbc.M109.042986).
- 750 31. Levi, S., Luzzago, A., Cesareni, G., Cozzi, A., Franceschinelli, F.,  
751 Albertini, A., and Arosio, P. (1988). Mechanism of ferritin iron uptake:  
752 activity of the H-chain and deletion mapping of the ferro-oxidase site. A  
753 study of iron uptake and ferro-oxidase activity of human liver,  
754 recombinant H-chain ferritins, and of two H-chain deletion mutants. *J Biol*  
755 *Chem* 263, 18086-18092.
- 756 32. Theil, E.C. (2013). Ferritin: the protein nanocage and iron biomineral in  
757 health and in disease. *Inorg Chem* 52, 12223-12233.
- 758 33. Lee, J.H., Gregory, A., Hogarth, P., Rogers, C., and Hayflick, S.J. (2018).  
759 Looking Deep into the Eye-of-the-Tiger in Pantothenate Kinase-  
760 Associated Neurodegeneration. *AJNR Am. J. Neuroradiol.* 39, 583-588.  
761 [10.3174/ajnr.A5514](https://doi.org/10.3174/ajnr.A5514).
- 762 34. Scola, E., Ganau, M., Robinson, R., Cleary, M., De Cocker, L.J.L.,  
763 Mankad, K., Triulzi, F., and D'Arco, F. (2019). Neuroradiological findings  
764 in three cases of pontocerebellar hypoplasia type 9 due to AMPD2  
765 mutation: typical MRI appearances and pearls for differential diagnosis.  
766 *Quant Imaging Med Surg* 9, 1966-1972. [10.21037/qims.2019.08.12](https://doi.org/10.21037/qims.2019.08.12).
- 767 35. Chiou, B., Neely, E.B., McDevitt, D.S., Simpson, I.A., and Connor, J.R.  
768 (2020). Transferrin and H-ferritin involvement in brain iron acquisition  
769 during postnatal development: impact of sex and genotype. *J.*  
770 *Neurochem.* 152, 381-396. [10.1111/jnc.14834](https://doi.org/10.1111/jnc.14834).
- 771 36. Fan, K., Jia, X., Zhou, M., Wang, K., Conde, J., He, J., Tian, J., and Yan,  
772 X. (2018). Ferritin Nanocarrier Traverses the Blood Brain Barrier and Kills  
773 Glioma. *ACS Nano* 12, 4105-4115. [10.1021/acsnano.7b06969](https://doi.org/10.1021/acsnano.7b06969).
- 774 37. Vidal, R., Ghetti, B., Takao, M., Brefel-Courbon, C., Uro-Coste, E.,  
775 Glazier, B.S., Siani, V., Benson, M.D., Calvas, P., Miravalle, L., et al.

- 776 (2004). Intracellular ferritin accumulation in neural and extraneural tissue  
777 characterizes a neurodegenerative disease associated with a mutation in  
778 the ferritin light polypeptide gene. *J. Neuropathol. Exp. Neurol.* **63**, 363-  
779 380. [10.1093/jnen/63.4.363](https://doi.org/10.1093/jnen/63.4.363).
- 780 38. Vidal, R., Delisle, M.B., and Ghetti, B. (2004). Neurodegeneration caused  
781 by proteins with an aberrant carboxyl-terminus. *J. Neuropathol. Exp.*  
782 *Neurol.* **63**, 787-800. [10.1093/jnen/63.8.787](https://doi.org/10.1093/jnen/63.8.787).
- 783 39. Cozzi, A., Orellana, D.I., Santambrogio, P., Rubio, A., Cancellieri, C.,  
784 Giannelli, S., Ripamonti, M., Taverna, S., Di Lullo, G., Rovida, E., et al.  
785 (2019). Stem Cell Modeling of Neuroferritinopathy Reveals Iron as a  
786 Determinant of Senescence and Ferroptosis during Neuronal Aging. *Stem*  
787 *Cell Reports* **13**, 832-846. [10.1016/j.stemcr.2019.09.002](https://doi.org/10.1016/j.stemcr.2019.09.002).
- 788 40. Girelli, D., Olivieri, O., De Franceschi, L., Corrocher, R., Bergamaschi, G.,  
789 and Cazzola, M. (1995). A linkage between hereditary hyperferritinaemia  
790 not related to iron overload and autosomal dominant congenital cataract.  
791 *Br. J. Haematol.* **90**, 931-934. [10.1111/j.1365-2141.1995.tb05218.x](https://doi.org/10.1111/j.1365-2141.1995.tb05218.x).
- 792 41. Beaumont, C., Leneuve, P., Devaux, I., Scoazec, J.Y., Berthier, M.,  
793 Loiseau, M.N., Grandchamp, B., and Bonneau, D. (1995). Mutation in the  
794 iron responsive element of the L ferritin mRNA in a family with dominant  
795 hyperferritinaemia and cataract. *Nat. Genet.* **11**, 444-446.  
796 [10.1038/ng1295-444](https://doi.org/10.1038/ng1295-444).
- 797 42. Kato, J., Kobune, M., Ohkubo, S., Fujikawa, K., Tanaka, M., Takimoto, R.,  
798 Takada, K., Takahari, D., Kawano, Y., Kohgo, Y., and Niitsu, Y. (2007).  
799 Iron/IRP-1-dependent regulation of mRNA expression for transferrin  
800 receptor, DMT1 and ferritin during human erythroid differentiation. *Exp.*  
801 *Hematol.* **35**, 879-887. [10.1016/j.exphem.2007.03.005](https://doi.org/10.1016/j.exphem.2007.03.005).
- 802 43. Cornell, T.A., Srivastava, Y., Jauch, R., Fan, R., and Orner, B.P. (2017).  
803 The Crystal Structure of a Maxi/Mini-Ferritin Chimera Reveals Guiding  
804 Principles for the Assembly of Protein Cages. *Biochemistry* **56**, 3894-  
805 3899. [10.1021/acs.biochem.7b00312](https://doi.org/10.1021/acs.biochem.7b00312).
- 806 44. Ingrassia, R., Gerardi, G., Biasiotto, G., and Arosio, P. (2006). Mutations  
807 of ferritin H chain C-terminus produced by nucleotide insertions have  
808 altered stability and functional properties. *J Biochem* **139**, 881-885.  
809 [10.1093/jb/mvj101](https://doi.org/10.1093/jb/mvj101).
- 810 45. Thompson, K., Menzies, S., Muckenthaler, M., Torti, F.M., Wood, T.,  
811 Torti, S.V., Hentze, M.W., Beard, J., and Connor, J. (2003). Mouse brains  
812 deficient in H-ferritin have normal iron concentration but a protein profile  
813 of iron deficiency and increased evidence of oxidative stress. *J Neurosci*  
814 *Res* **71**, 46-63. [10.1002/jnr.10463](https://doi.org/10.1002/jnr.10463).
- 815 46. Sobreira, N., Schiettecatte, F., Valle, D., and Hamosh, A. (2015).  
816 GeneMatcher: a matching tool for connecting investigators with an  
817 interest in the same gene. *Hum. Mutat.* **36**, 928-930.  
818 [10.1002/humu.22844](https://doi.org/10.1002/humu.22844).
- 819
- 820

## 821 **Figure Titles and Legends**

822 Figure 1. Neuroimaging findings of individuals with heterozygous *FTH1* variants.  
823 Proband 1: 11-15 years old female brain MRI (A-C), and baseline brain MRI  
824 when she was 6-10 years old (D). (A) Sagittal T1WI shows severe hypoplasia  
825 and atrophy of the vermis along with a diffusely thin corpus callosum. (B) Axial  
826 SWI shows artifacts within the globus pallidi corresponding to abnormal areas of  
827 iron deposition (arrow, B). (C) Axial T2WI demonstrate selective hyperintense  
828 signal involving the anterior segment of the globus pallidi, giving the eye of tiger  
829 sign (arrowhead, C), feature not observed in the baseline MRI axial T2WI, 5  
830 years before (D). Proband 3: 0-5 years old female brain MRI (E-I) (E) Sagittal  
831 T1WI shows severe pontocerebellar hypoplasia along with a diffusely thin corpus  
832 callosum. Axials gradient echo, and magnetization transfer T1 show dark artifacts  
833 (F) and T1 shortening (G) within the basal ganglia corresponding to abnormal  
834 areas of mineralization (arrows, F, and G) along with severe white matter volume  
835 loss. Severe atrophy of the midbrain giving a “figure 8” appearance of this  
836 structure (dotted circle, H) and T2 crossed linear hyperintensities (arrowhead I),  
837 representing the hot-cross bun sign.

838  
839 Figure 2. Neuropathology and ferritin staining. Representative H&E images from  
840 (A) frontal cortex show intracellular inclusions (arrow) (B) NeuN  
841 immunohistochemistry showing intracellular inclusions present in neurons  
842 (arrow). There was patchy iron deposition shown in the basal ganglia by Prussian  
843 blue stain (arrowhead) (C), and the inclusions immunostained for ferritin heavy  
844 chain protein FTH1 (arrow) (D,E). Negative control: unaffected brain (F).  
845 Magnification is 400x (A-D) and 200x (E-F), scale bar is 20  $\mu\text{m}$ .

846  
847 Figure 3. *FTH1 de novo* variant effects on ferritin heavy and light chain protein  
848 and mRNA levels. A-B) Quantification of protein levels and representative  
849 immunoblots showing FTH and FTL protein levels in primary patient-derived  
850 fibroblasts (filled circles) vs controls (open circles). All *FTH1*-variant cells (shown  
851 as P1, P2, P3) showed elevated levels of both light and heavy chains of ferritin  
852 relative to controls. Quantification was analyzed by genotype using two  
853 independent cell lines per genotype, except P1 which is the only available line  
854 with the p.S164\* variant [P1= *FTH1* c.487\_490 dupGAAT (p.S164\*); P2 and

855 P3= *FTH1* c.512\_513delTT, (p.F171\*), Controls=FTHctrl and Coriell 8400 lines].  
856 C) Quantification of total *FTL* and *FTH1* mRNA transcripts by RT-PCR in patient  
857 fibroblasts relative to controls (mean levels relative to control=1: P1 0.778±0.05,  
858 P2 0.825±0.06). D) RT-PCR for allele-specific *FTH1* mRNA transcripts,  
859 performed for each genotype. *FTH1* mutant transcripts are detectable with  
860 mutation-specific primers in patient fibroblasts. In P1, mutant transcript levels  
861 were higher than wild type transcripts, while in P2, wild type levels were higher  
862 than mutant transcript. In both genotypes, however, the data demonstrate that  
863 nonsense mutant transcripts were present and escape nonsense mediated  
864 decay. All data represented as mean ± SEM; Data analyzed with one way Anova  
865 with Tukey's multiple comparisons test; \*p<0.05, \*\*p<0.01, \*\*\*p<0.001,  
866 \*\*\*\*p<0.0001

867

868

869 Figure 4: Immunocytochemistry for ferritin subcellular localization (A-D). Cells  
870 were stained with anti-FTL (green), anti-FTH (red), lysosomal LAMP1 (white),  
871 and nuclear stain DAPI (blue). Scale bar = 5 µm. For exogenous iron treatment  
872 (+Fe), cells were treated with 150 µg/mL FAC for 3 days.

873

874

875 Figure 5. Iron Content and Oxidative Stress Markers. A) Iron exposure  
876 experiments in patient-derived cells and iron quantification. Fibroblasts were  
877 treated with FAC, 150 µg/mL for 3 or 7 days and assayed with inductively  
878 coupled plasma optical emission spectroscopy (ICP-OES) as described. Dark  
879 grey base bars are untreated controls for each cell line. B) Oxidative stress  
880 assay: oxyblot immunodetection of carbonyl groups, quantified by densitometry  
881 in control vs patient cells. C) Lipid peroxidation levels were assayed with C11-  
882 BODIPY<sup>581/591</sup> and quantified by plate reader. For most assays n≥2 cell lines per  
883 genotype (except for P1 as only one line available); for each cell line assays with  
884 technical triplicates. All data represent mean ± SEM. \*p<0.05, \*\*p<0.01,  
885 \*\*\*p<0.001.

886

887

888 Figure 6: Structural modeling of *FTH1* *de novo* variants predict truncation of E-  
889 helix (circle) and are predicted to affect ferritin's pore size (arrow head) for  
890 p.S164\* variant and pore depth (not evident in the schematic, but the depth of  
891 the pore is predicted to be 4.5 Å shallower than wild-type due to the missing  
892 terminal residues) for p.F171\* variant.

893

894 Figure 7. Antisense oligonucleotides (ASO) directed toward *FTH1* variant in  
895 Proband 1 (c.487\_490 dupGAAT, p.Ser164\*) in fibroblasts. (A) RT-PCR was  
896 used to detect the mutant allele specifically, verifying its detection in patient  
897 fibroblasts but not in control. The P1 targeted ASO specifically suppressed  
898 expression of the mutant allele and not wild type. (B) Treating P1 cells with the  
899 ASO restored lipid peroxidation levels, while scrambled (SCR) control had no  
900 effect (n=3 experiments with ≥4 technical replicates per group). (C) ASO reduces  
901 ferritin heavy chain protein to near control levels. All data represented as mean ±  
902 SEM; Data analyzed with one way Anova with Tukey's multiple comparisons test;  
903 \*p<0.05, \*\*p<0.01, \*\*\*p<0.001, \*\*\*\*p<0.0001

904

905

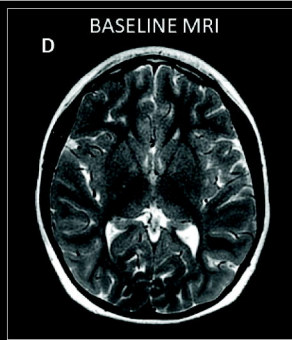
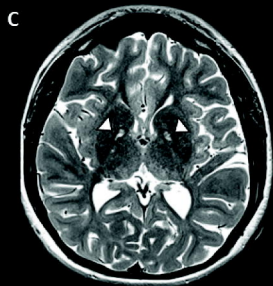
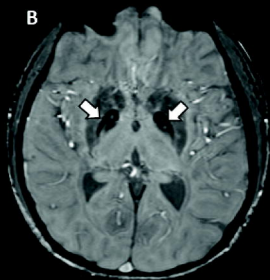
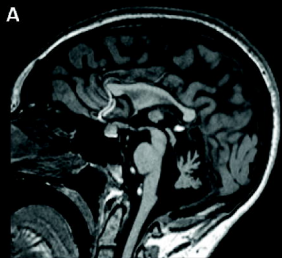
**Table 1: Clinical features of unrelated individuals with heterozygous *FTH1* variants\***

\*details edited/removed to comply with Medrxiv policies, ages provided in ranges

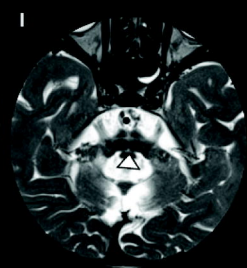
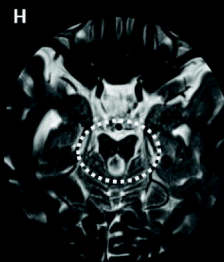
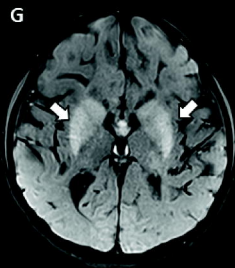
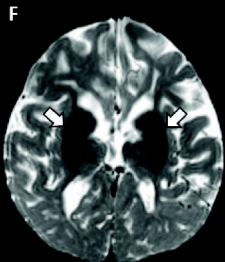
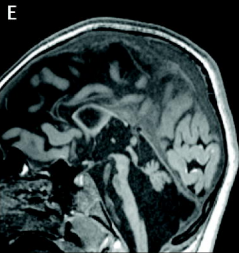
<b>Parameter</b>	<b>Pt 1</b>	<b>Pt 2</b>	<b>Pt 3</b>	<b>Pt 4</b>	<b>Pt 5</b>
Age at last evaluation, sex	11-15yr, F	16-20yr, F	0-5yr, F	0-5 yr, F	11-15yr, F
<b>Neurologic Symptoms</b>					
Dysphagia	no	yes	yes	yes	Yes
Involuntary movements	mild dystonic posturing	dystonia, athetosis	yes	startle	Startle
Epilepsy	yes	single seizure	yes	no	No
EEG	multifocal sharp waves, more frequent right posterior	generalized background slowing	right posterior sharps, myoclonic seizures	abnormal background without interictal discharges during sleep/wake	No epileptiform activity
<b>Neuroimaging</b>					
White matter	abnormal	abnormal	abnormal, PCH	abnormal	Abnormal
Cerebellum	hyper T2 periventricular	decreased	decreased	decreased	Supratentorial white matter volume loss
MRI SWI+ signal abnormalities	progressive atrophy	hypoplasia, progressive atrophy	hypoplasia	hypoplasia	atrophy
Basal ganglia abnormal	yes	yes	no	yes, not intraparenchymal (likely due to birth)	
Genetics/Diagnostics	yes	yes	yes	yes	yes
<b>Metabolic testing</b>					
Metabolic testing	hi lactate/pyruvate ratio: nl pl aa, acp, uoa	minimal lactate, Wilson nl			NI uoa, acp
Other genetic tests	SNP 7q31.1 del VUS	Rett, Angelman, Fragile X nl	SNP normal	SNP 8p12 dup VUS, 12p12.1 del VUS	SNP normal
<b>Whole exome</b>					
<i>FTH1</i> variant type	Truncation	Truncation	Truncation	Truncation	Truncation
cDNA, protein position	c.487_490 dupGAAT, p.Ser164*, de novo	c.512_513delTT, p.Phe171*, de novo	c.512_513delTT, p.Phe171*, not mat	c.512_513delTT, p.Phe171*, de novo	c.512_513delTT p.Phe171*, de novo
<b>Systemic/Labs</b>					
Ophthalmologic	normal (9yr)	abnormal	nd	abnormal	Cortical visual impairment
CV/Renal involvement	no	no	no	no	No
GI/constipation	N/A	yes	yes	yes	Enteral feeds
LFTs	normal	normal	normal	N/A	
<b>Iron Studies</b>					
Ferritin, ng/mL (reference)	7.9 (10-150)	6 (12-114)	10.6 (13-150)	50.7 (5.3-99.9)	162 (6-67)
Serum iron, ug/dL	28 (28-147)	35 (29-189)	47 (33-151)	15.5 (4.8-25.4 umol/L)	111 (27-164)
TIBC, ug/dL (reference)	391 (250-450)	nd	588 (250-425)	nd	252 (271-448)
Transferrin saturation (%)	11 (20-50)	9 (10-47)	8 (15-55)	nd	44 (15-45)
Hemoglobin, g/dL	10.3	11.3	10	12.6	14.1



Proband 1

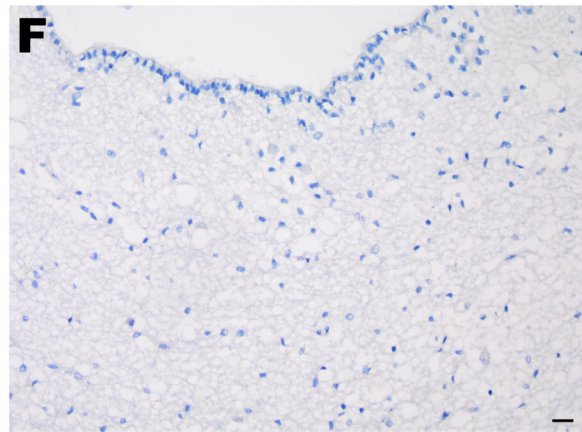
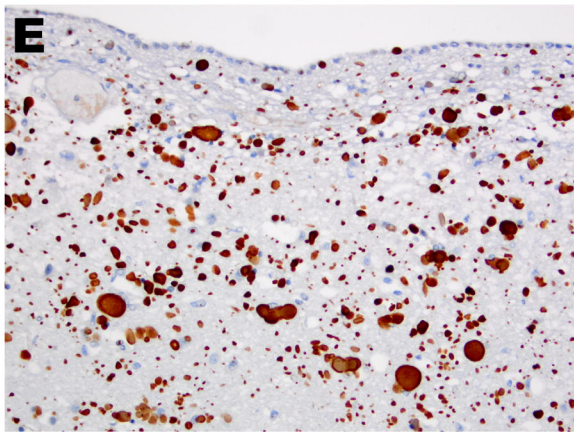
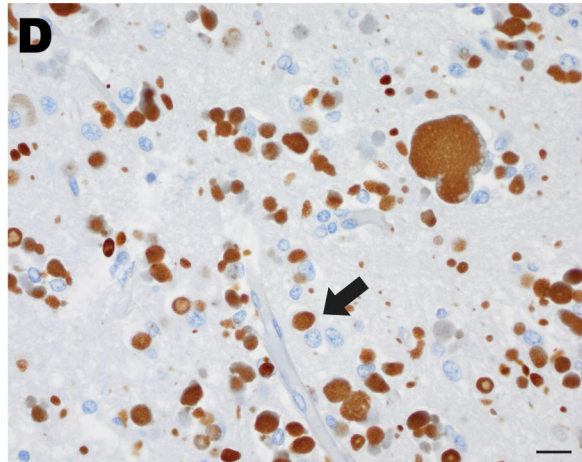
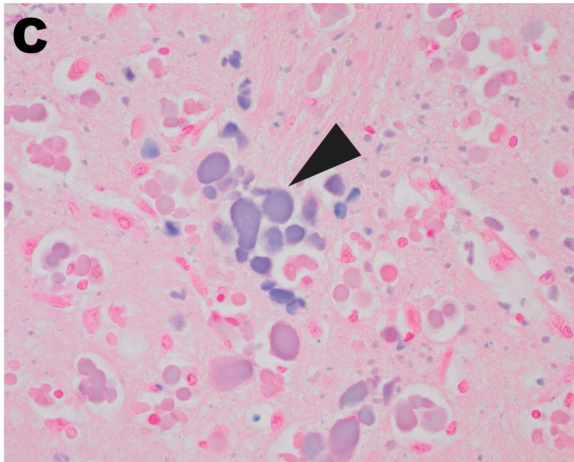
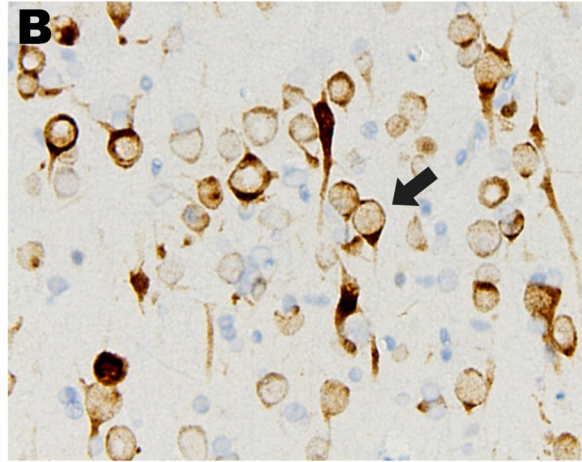
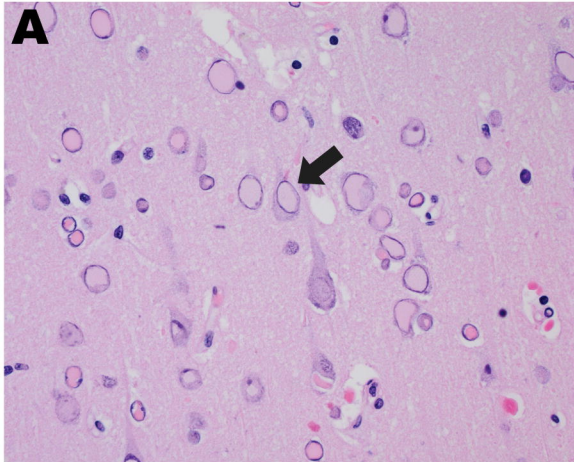


Proband 3





**Fig 2**



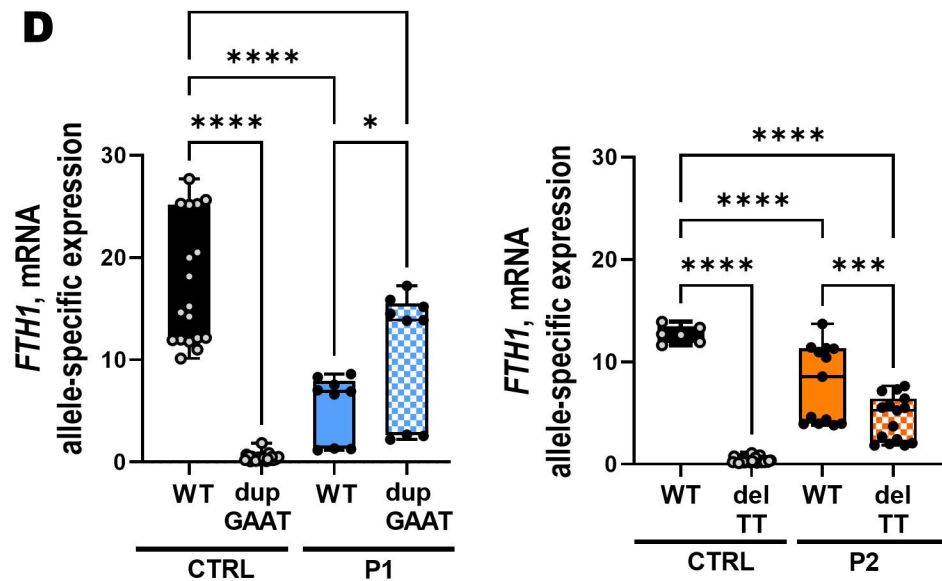
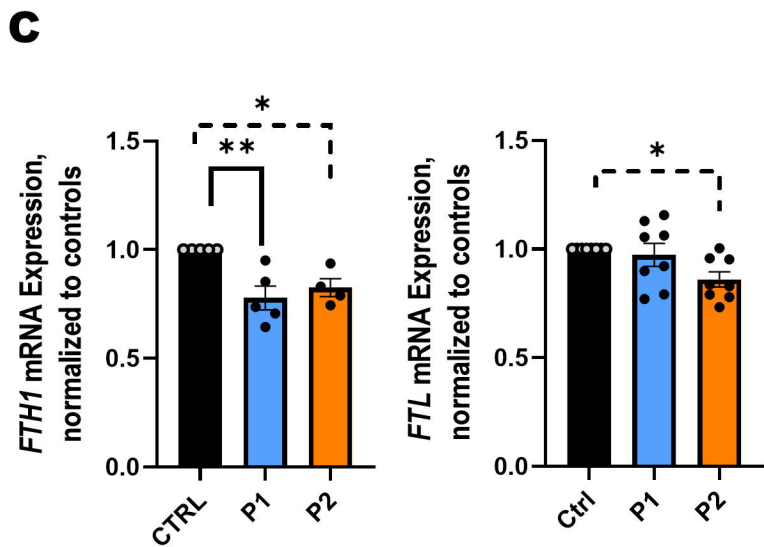
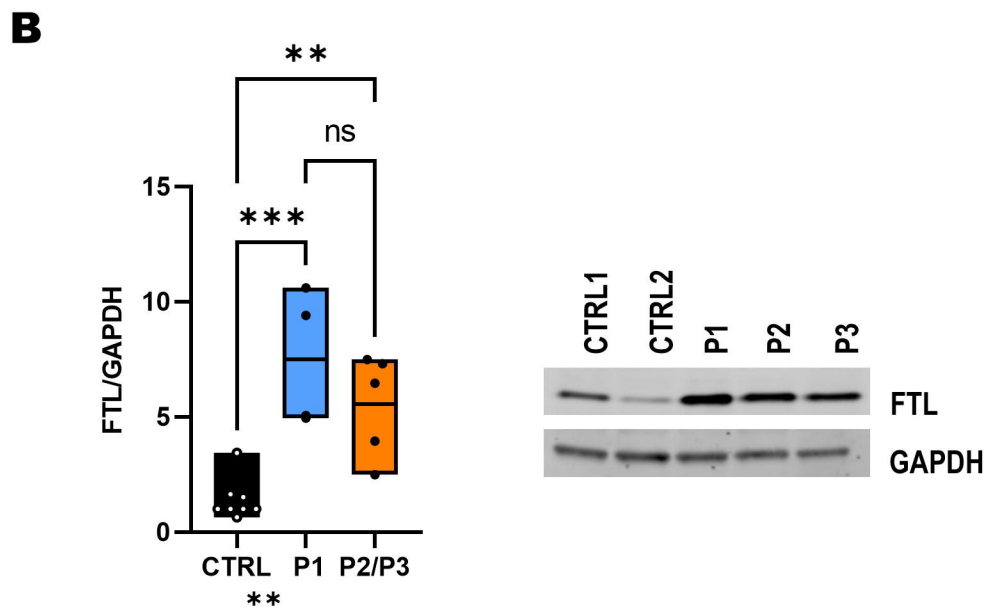
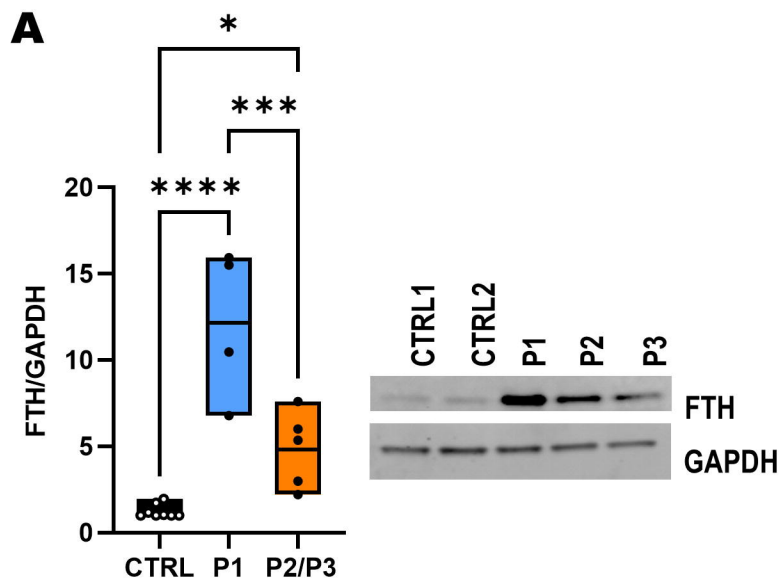


**Fig 4**

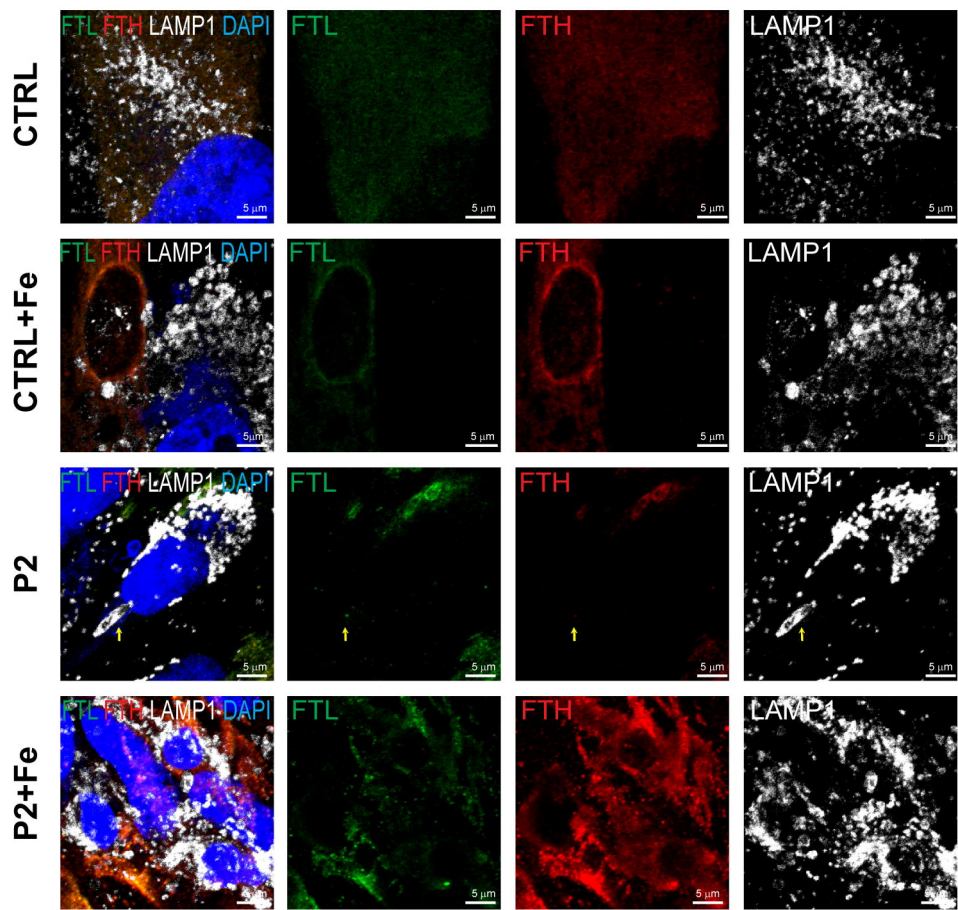
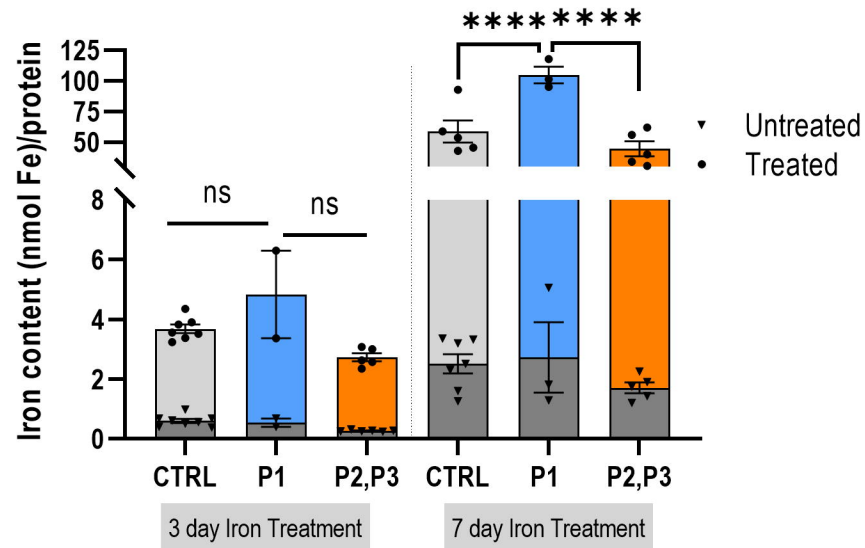
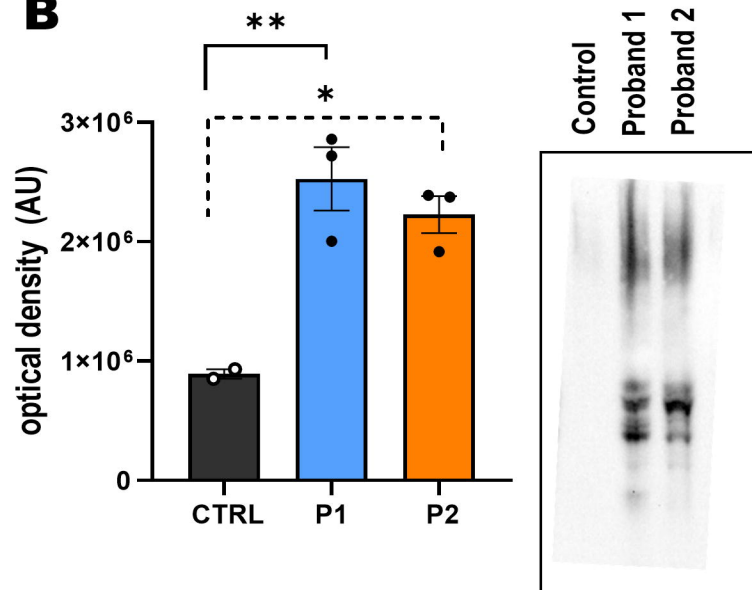


**Fig 5**

**A**



**B**



**C**

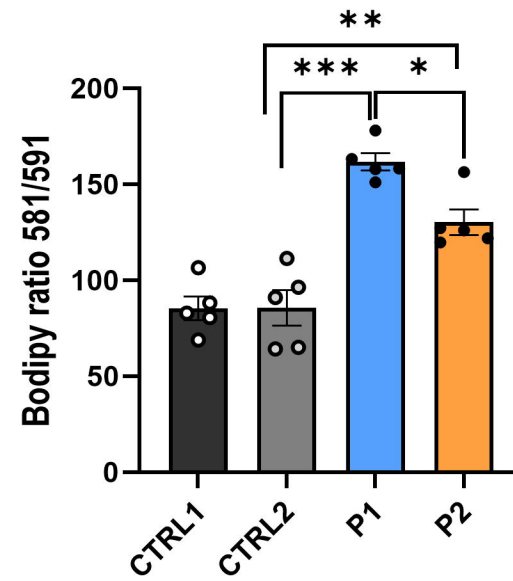




**Fig 6**

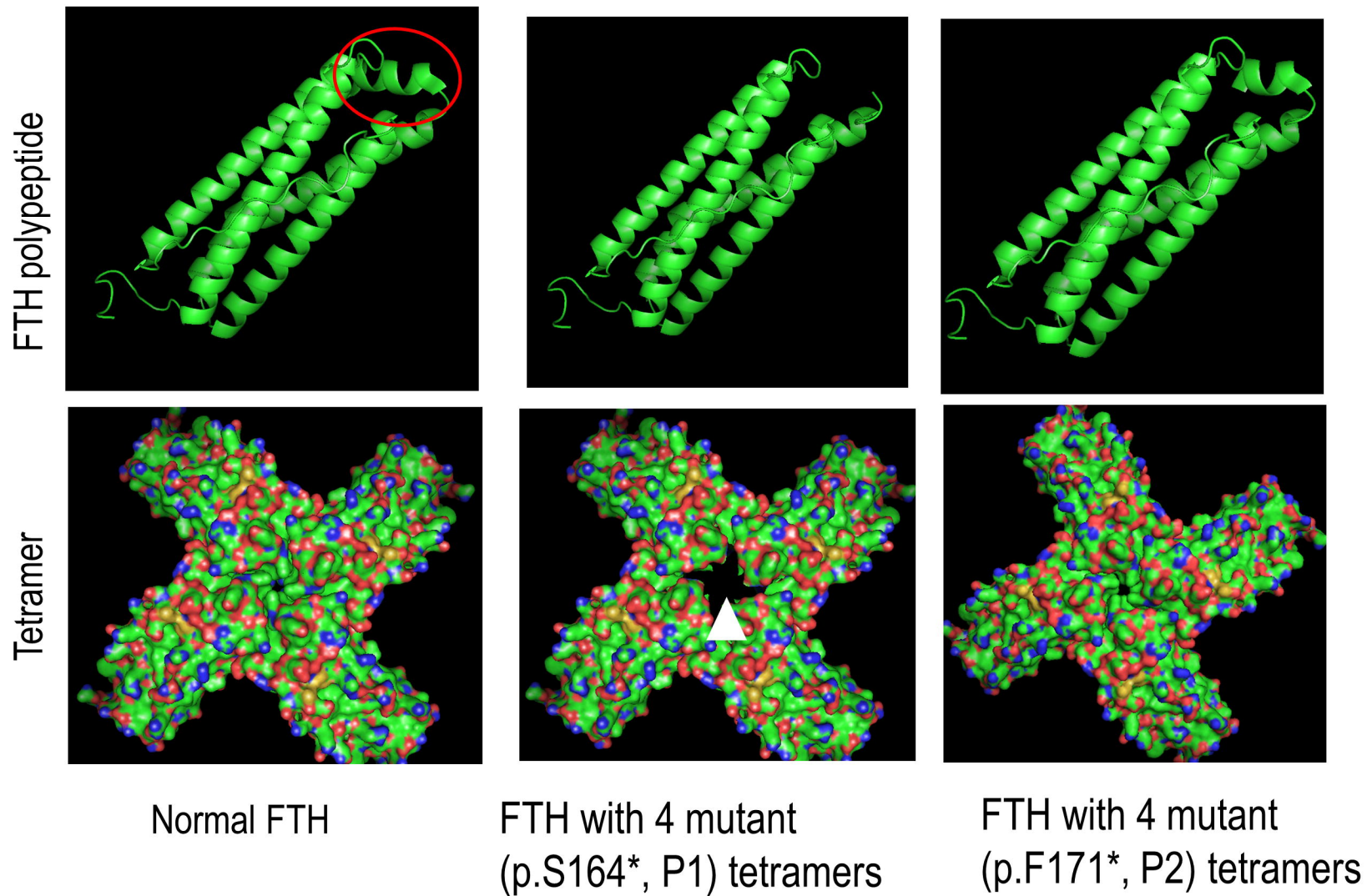


**Fig 7**

